

# Soft Matter

Accepted Manuscript



This is an Accepted Manuscript, which has been through the Royal Society of Chemistry peer review process and has been accepted for publication.

Accepted Manuscripts are published online shortly after acceptance, before technical editing, formatting and proof reading. Using this free service, authors can make their results available to the community, in citable form, before we publish the edited article. We will replace this Accepted Manuscript with the edited and formatted Advance Article as soon as it is available.

You can find more information about Accepted Manuscripts in the [Information for Authors](#).

Please note that technical editing may introduce minor changes to the text and/or graphics, which may alter content. The journal's standard [Terms & Conditions](#) and the [Ethical guidelines](#) still apply. In no event shall the Royal Society of Chemistry be held responsible for any errors or omissions in this Accepted Manuscript or any consequences arising from the use of any information it contains.



# Journal Name

## ARTICLE TYPE

Cite this: DOI: 10.1039/xxxxxxxxxx

## Structure and cohesive energy of dipolar helices

Igor Stanković,<sup>\*a</sup> Miljan Dašić,<sup>a</sup> and René Messina<sup>b</sup>

Received Date

Accepted Date

DOI: 10.1039/xxxxxxxxxx

[www.rsc.org/journalname](http://www.rsc.org/journalname)

This paper deals with the investigation of cohesive energy in dipolar helices made up of hard spheres. Such tubular helical structures are ubiquitous objects in biological systems. We observe a complex dependence of cohesive energy on surface packing fraction and dipole moment distribution. As far as *single helices* are concerned, the lowest cohesive energy is achieved at the highest surface packing fraction. Besides, a striking non-monotonic behavior is reported for the cohesive energy as a function of the surface packing fraction. For *multiple helices*, we discover a new phase, exhibiting a pronounced deep cohesive energy. This phase is referred to as *ZZ tube* consisting of stacked crown rings (reminiscent of a pile of zig-zag rings), resulting in a local triangular arrangement with densely packed filaments parallel to the tube axis.

### 1 Introduction

Particles with permanent dipole moments, such as magnetic particles, are well known for their outstanding self-assembly properties<sup>1–3</sup>. In biology, tubular and helical structures are relevant self-assembled objects for instance found in bacterial flagella<sup>4</sup> and microtubules<sup>5,6</sup>. Other instances of such tubular/helical structures can be found in various materials with specific building units that can be: carbon atoms<sup>7</sup>, coiled carbon nanotubes<sup>8</sup>, DNA<sup>9</sup>, nanoparticles<sup>10</sup>, or amphiphilic molecules<sup>11–13</sup>. Self organizing of cubic magnetic nanoparticles<sup>14</sup> and asymmetric colloidal magnetic dumbbells<sup>15</sup> into helical architectures were recently reported without need of preexisting template.

On a more theoretical side, hard spherical particles confined into narrow cylinders spontaneously assemble into helical structures<sup>16,17</sup> and also seen experimentally<sup>18</sup>. Hard-spheres with permanent moment can be employed as a paradigm for more complex helical molecular superstructures<sup>19</sup>, or microtubules<sup>20,21</sup>. The pioneering theoretical work of Jacobs and Beans<sup>22</sup> and later that of de Gennes and Pincus<sup>23</sup> shed some light on the microstructure of self-assembled unconstrained (spherical) dipoles. More recently, the paper<sup>24</sup> advocated the ground states of self-assembled magnetic structures. The authors proved

that for a sufficiently high number of particles the ground state is obtained via ring stacking into tubes<sup>24</sup>. On the other hand Vella et al.<sup>25</sup> showed an illustrative example in which a macroscopic straight portion of the chain spontaneously wraps itself building a tube. At larger scales, Janus chain model was able to well reproduce formation of superstructures and double helical conformations of amphiphilic molecules<sup>26,27</sup>. The competition between toroidal and rod-like conformations, as possible ground states for DNA condensation, was studied using a polymer chain model function of stiffness and short range interactions<sup>28,29</sup>. Also introduced recently, polymorphic dynamics model<sup>30,31</sup> was able to reproduce behavior of the microtubule lattice based on rough understanding of underlying atomic level processes. The general scientific problem of understanding the processes by which building blocks (dipoles) self assemble and obtain their functionality is highly challenging<sup>32–36</sup>.

The goal of this paper is to address the intimate link between microstructure and cohesive energy. Tubular helical structures can be obtained either (i) through ring stacking or (ii) by rolling of one or multiple helices on a confining cylindrical surface (in Sec. 2). The dipolar interaction model is introduced and a link between dipole distribution the microstructure established in Sec. 3. In Sec. 4, starting from the most simple case corresponding to a single helix, we discuss the relation between surface packing and the resulting macroscopic properties such as the cohesive energy or the overall polarization. Then, the more complex situation of multiple helices with densely packed constitutive particles is ad-

<sup>a</sup> Scientific Computing Laboratory, Institute of Physics Belgrade, University of Belgrade, Pregrevica 118, 11080 Belgrade, Serbia. E-mail: igor.stankovic@ipb.ac.rs

<sup>b</sup> Institut de Chimie, Physique et Matériaux (ICPM), Université de Lorraine, 1 Bd. Arago, 57070 Metz, France.

† Corresponding author.

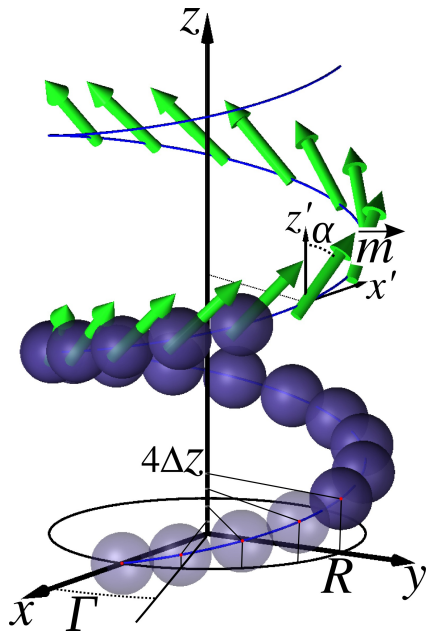


**Fig. 1** Illustration of a single helix with relevant geometrical parameters ( $R, \Gamma, \Delta z$ ) labelled. The bold line connecting spherical particle centers represents backbone of the helix. In upper part of the figure, the azimuthal dipole moment orientation  $\alpha$  is defined in a local coordinate system with its origin corresponding to the particle center. The  $z'$ -axis is parallel to the cylinder axis.

dressed. There, the alignment degree (especially in the ground state) between dipole moment orientation and helix axis is analyzed.

## 2 Geometry of helices

### 2.1 Geometry of the single helix

In the framework of this paper, helices are composed of hard spherical particles and confined on a cylinder's surface, i.e., the helices are created by rolling threads on the cylindrical surface of radius  $R_{cyl}$ . Geometrical parameters that define a single helix are: azimuthal angular shift  $\Gamma$  between the centers of two successive particles and radius of the helix  $R = R_{cyl} + d/2$ , where  $d$  stands for the hard sphere diameter, see Fig. 1. The radius  $R$ , represents physically the distance of the closest approach between cylinder axis and center of the spherical particle.

The Cartesian coordinates of particle  $i$  in a single helix are calculated as:  $x_i = R\cos(i\Gamma)$ ,  $y_i = R\sin(i\Gamma)$ , and  $z_i = i\Delta z$ , where  $i \in \mathbb{Z}$  and assuming that one particle is at  $(x, y, z) = (R, 0, 0)$ . Distance between the centers of each two successive particles along the helix axis is labelled as  $\Delta z$ , see Fig. 1. When constructing a helix, its radius  $R$  and azimuthal angular distance  $\Gamma$  have to be chosen in a way which ensures non-overlapping of hard spheres. Non-overlapping constraint is expressed for any two particles  $i, j$  as

$|\vec{r}_{ij}| \geq d$ . Since the helix thread is everywhere connected, any two successive particles are touching. We can obtain  $\Delta z$  as a function of other two variables:  $\Delta z = \sqrt{d^2 + 2(\cos\Gamma - 1)R^2}$ . Thereby, variables  $\Delta z$ ,  $R$  and  $\Gamma$  are not independent. Clearly, with decreasing  $\Delta z$  (i.e., increasing  $\Gamma$ ) helices become more compact. Because of connectivity, every particle in a helix has at least two neighbors, i.e., the coordination number,  $n_c$ , is always greater or equal than two ( $n_c \geq 2$ ). The highest packing density of the particles for prescribed confinement radius  $R$  will be achieved when successive helix turns touch. In this situation of touching turns, the coordination number  $n_c$  can be either four or six. Therefore, in general,  $n_c \in \{2, 4, 6\}$ , where the case  $n_c = 2$  corresponds to non-touching turns. Based on the coordination number  $n_c$ , we can classify helices as follows (see Fig. 2a-c). Examples of helices with two neighbors  $n_c = 2$  and four neighbors  $n_c = 4$  at prescribed cylindrical confinement, e.g.,  $R/d = 1.78$ , are sketched in Fig. 2a and b, respectively. For a number of well-defined radii, as discussed later in this paper, densely packed helices with six neighbors ( $n_c = 6$ ) can be formed, see Fig. 2c. In the following sections, we will also investigate stacked rings forming so called tubes also depicted in Fig. 2d-f.

### 2.2 Order parameters for single helices

The surface packing fraction,  $\eta = S/S_{\text{avail}}$ , is defined as the ratio of the area  $S = \pi d^2/4$  covered by one particle and the area available for one particle  $S_{\text{avail}}$ , in an unrolled configuration.

Following the definition of the surface packing density we obtain †:

$$\eta = \frac{d^2}{8\Delta z R}. \quad (1)$$

For comparison we are going also to derive packing fraction for the tubes ‡:

- Surface packing fraction of AA tubes is given by  $\eta_{\text{AA}} = N_{\text{ring}}d/8R_{\text{AA}}$  for AA tube with  $N_{\text{ring}}$  particles per ring and confinement radius  $R_{\text{AA}}/d = 1/[2\sin(\pi/N_{\text{ring}})]$ , see Fig. 2d for a microstructure with  $R_{\text{AA}}/d = 1.93$ .
- Similarly, for AB tubes, the packing fraction is  $\eta_{\text{AB}} = N_{\text{ring}}d^2/8R_{\text{AB}}\Delta z_{\text{AB}}$ , with  $R_{\text{AB}} = R_{\text{AA}}$ . Here, the elevation

† The available area per particle is  $S_{\text{avail}} = 2\pi R\Delta z$ , where distance between successive particles along tube axis is  $\Delta z$ . We take for surface covered by particle  $S = \pi d^2/4$ , i.e., neglecting curvature. This results in a small overestimation of packing fraction (less than 2% for large curvatures, e.g.,  $R/d = \sqrt{3}/2$ ).

‡ The tubes are obtained via ring stacking. It is convenient to calculate surface packing fraction as the ratio of the area covered by the particles in a unit ring and the available area per ring. The surface covered is  $S = N_{\text{ring}}\pi d^2/4$ . The available area per ring is  $S_{\text{avail}} = 2\pi R\Delta z$  where  $\Delta z$  is distance between successive rings. The distance between successive rings is  $\Delta z = d$  for AA and ZZ tubes.

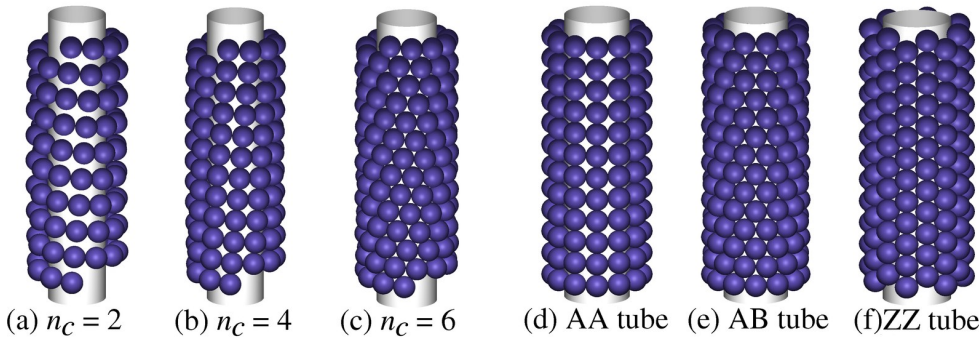


**Fig. 2** Illustration of different classes of helices, based on coordination number  $n_c = 2, 4, 6$ . (a) Helix with *non-touching* turns ( $n_c = 2$ ). (b) Helix with touching turns ( $n_c = 4$ ). (c) Densely packed helix ( $n_c = 6$ ). The other panels illustrate, so called, (d) AA, (e) AB, and (f) ZZ tubes. The tubes can be created by strict axial stacking of unit rings. For AA and AB tubes unit rings are flat, whereas, for ZZ tubes the unit ring has a crown shape (reminiscent of pile of 'zig-zag' rings). The radii of AA and AB tubes are the same  $R/d = 1.93$ .

$\Delta z_{AB}$  between two consecutive rings is:

$$\Delta z_{AB} = (d/2) \sqrt{2 + 2 \cos(\pi/N) - \cos^2(\pi/N)}. \quad (2)$$

- For ZZ tubes, the packing fraction is  $\eta_{ZZ} = N_{\text{ring}} d / 8R_{ZZ}$ , with confinement radius  $R_{ZZ}/d = \sqrt{3}/[4 \sin(\pi/N_{\text{ring}})]$ .

To further characterize the helical microstructures, we introduce an additional geometrical order parameter  $\xi$  which is valid for  $n_c = 4$  and 6. This order parameter connects an individual reference particle 0 located at  $\vec{r}_0$  in the helix with its two neighbors: its immediate successive particle 1 in the turn ( $\vec{r}_{01} = \vec{r}_1 - \vec{r}_0$ ) and a neighboring particle 2 from the next turn ( $\vec{r}_{02} = \vec{r}_2 - \vec{r}_0$ ), see Fig. 3(a).

The *angular coordination order parameter* is conveniently defined as:

$$\xi = 2 \frac{|\vec{r}_{01} \cdot \vec{r}_{02}|}{d^2}. \quad (3)$$

In the two limiting cases, the angular coordination order parameter has values:  $\xi_{\min} = 0$ , for a locally square lattice on a cylinder (e.g., AA tubes, check Fig. 2d) and  $\xi_{\max} = 1$ , for a locally triangular lattice (e.g. AB tubes, check Fig. 2e). In all other cases, the value of angular coordination order parameter  $\xi$  is between those two extremal values, i.e.,  $0 \leq \xi \leq 1$ .

### 2.3 Multiple helices at high surface packing fraction

The densely packed helices ( $n_c = 6$ ) can be created, in analogy to carbon nanotubes, by rolling a ribbon of a triangular lattice on a cylinder surface<sup>37</sup>. We deal with cylindrical geometry, infinite in one direction. We can generate these helical structures by periodical reproduction of a *curved patch* (unit cell) along the helical line with *spanning vectors* ( $\vec{a}_1, \vec{a}_2$ ). This curved unit cell has  $n_1$

particles along  $\vec{a}_1$  direction and  $n_2$  particles in  $\vec{a}_2$  direction. §

Since we deal with hard spheres and we aim to build very dense structures, the parameter space  $(R, \Delta z, n_1, n_2)$  is significantly restricted. We are going to find out that only two of these parameters are independent. There exists relation linking elevation angle  $\Theta = \arcsin(\Delta z/d)$  and confinement radius  $R$ , see Ref.<sup>37</sup>. Bearing in mind that for any pair  $(n_1, n_2)$  or equivalently  $(n_2, n_1)$ , we have a unique corresponding structure with  $n_c = 6$ , one arrives at the two following independent equations:

$$\Theta(n_1, n_2) = \arctan \left( \frac{\sqrt{3}n_2}{2n_1 + n_2} \right) \quad (4)$$

and

$$180^\circ = n_1 \arcsin \left[ \left( \frac{d}{4R} \right) \frac{2n_1 + n_2}{\sqrt{n_1^2 + n_2^2 + n_1 n_2}} \right] + \\ n_2 \arcsin \left[ \left( \frac{d}{4R} \right) \frac{2n_2 + n_1}{\sqrt{n_1^2 + n_2^2 + n_1 n_2}} \right]. \quad (5)$$

We have solved those two equations and obtained the set  $(\Theta, R/d)$  shown in Fig. 4. For each value of  $R$  there are two different values of  $\Theta$ , symmetric around  $\Theta = 30^\circ$ , which correspond to lattice constant pairs  $(n_1, n_2)$  and  $(n_2, n_1)$ , respectively. The  $(n_1, n_2)$  pairs are actually identical structures with opposite chirality<sup>38</sup>. The six-fold rotational symmetry of the lattice restricts  $\Theta \in [0^\circ, 60^\circ]$ .

We look now into properties of  $(n_1, n_2)$  pairs in order to char-

§ The values  $n_1$  and  $n_2$  can be seen as the two possible widths of the ribbon generating the same helical structure.

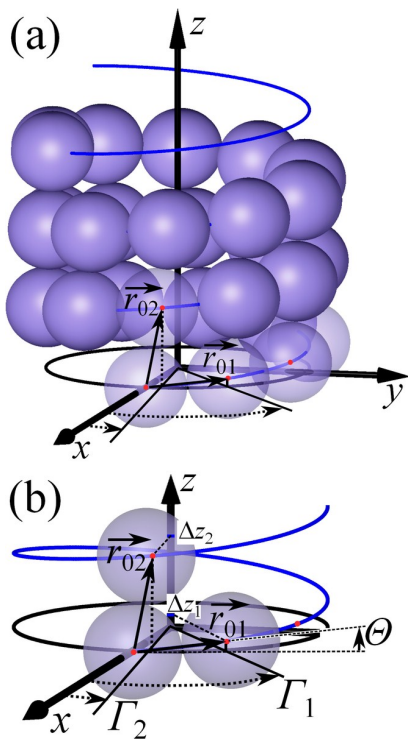


**Fig. 3** (a) Illustration of a helix made of hard spheres, helix backbone (solid line), and the vectors connecting a reference particle 0 located at  $(x, y, z) = (R, 0, 0)$  with its neighbors: an immediate successive particle 1 in the turn located at  $(\vec{r}_{01})$  and a neighboring particle 2 from the next thread turn at  $(\vec{r}_{02})$ . (b) Overview of the principal geometrical parameters of  $n_c = 4, 6$  helices: elevation angle  $\Theta$  and azimuthal angular shifts  $\Gamma_1$  and  $\Gamma_2$  (see Eq. 7). In our notation, densely packed directions along helical superstructure are called threads. The corresponding elevation distances of successive particles along helix axes  $\Delta z_{1,2}$  (see Eq. 9) are also given for two possible rollings of the same helix configuration.

acterize multi thread structure of six neighbor helices ( $n_c = 6$ ). First, we identify the link between  $n_c = 6$ -tubes and the  $(n_1, n_2)$  pair values. The pairs  $(0, n_2)$  and  $(n_1, 0)$  leading to  $\Theta = 60^\circ$  and  $0^\circ$ , respectively, represent *AB tubes*, cf. Fig. 4. The pairs with  $n_1 = n_2$  corresponding to  $\Theta = 30^\circ$  lead to *ZZ tubes* that are characterized as constitutive straight filaments parallel to the ZZ tube axis, see Fig. 2f. The curve with  $n_1 = 1$  (with  $n_2 \geq 3$ ) corresponds to a single helix,  $n_1 = 2$  (with  $n_2 \geq 3$ ) to a double helix,  $n_1 = 3$  (for any  $n_2 \geq 4$ ) to a triple helix, and more generally a  $n_1$ -helix structure is obtained when  $n_2 \geq n_1 + 1$ .

We employ Cartesian coordinates to express positions of particles in a  $n$ -helix similarly to the single helix case, using two

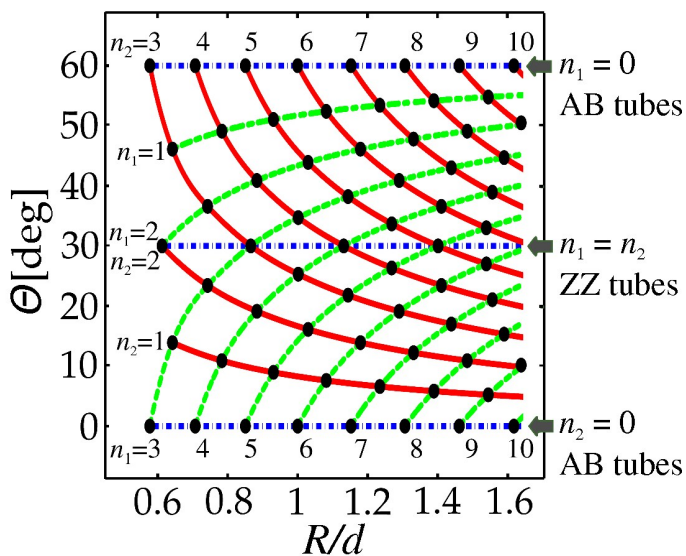


**Fig. 4** Phase diagram in the  $(\Theta, R/d)$ -plane showing possible unit cells characterized by  $(n_1, n_2)$  pairs. Solid lines represent unit cells with  $n_2$  fixed, and the dashed ones represent unit cells with  $n_1$  fixed. The three horizontal lines (dot-dashed) correspond to tubes.

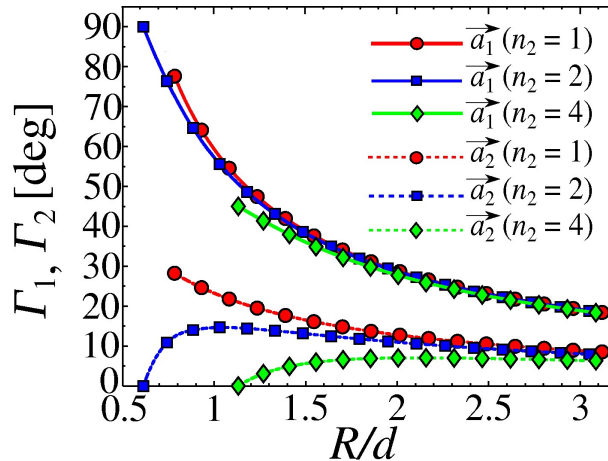


**Fig. 5** Dependence of azimuthal angular shift parameters  $\Gamma_1, \Gamma_2$  stemming from corresponding spanning vectors  $\vec{a}_1, \vec{a}_2$ , respectively, on reduced helix radius  $R/d$ , for single ( $n_2 = 1$ ), double ( $n_2 = 2$ ), and quadruple ( $n_2 = 4$ ) helices.

indices,  $i \in Z$  and  $j = \{1, n\}$ :

$$\begin{aligned} x_{i+jn} &= R \sin(i\Gamma_1 + j\Gamma_2) \\ y_{i+jn} &= R \cos(i\Gamma_1 + j\Gamma_2) \\ z_{i+jn} &= i\Delta z_1 + j\Delta z_2. \end{aligned} \quad (6)$$

¶ In our notation, multiple helices are named after the smallest unit patch dimension, i.e., the smallest number of generating threads.

In Eq. 6,  $\Gamma_1$  represents azimuthal angular shift between each two consecutive particles along a given thread and  $\Gamma_2$  is angular shift between threads, i.e., densely packed directions in superstructure, see Fig. 3(b). The azimuthal angle  $\Gamma_1$  is merely provided by :

$$\Gamma_1 = \arccos \left[ 1 - \left( \frac{d}{\sqrt{2}R} \cos \Theta \right)^2 \right]. \quad (7)$$

The angular shift  $\Gamma_2$  between threads is more delicate to derive. Knowing that starting from reference particle the same particle position is possible to reach following two paths along threads (in  $\vec{a}_1$ - or  $\vec{a}_2$ -direction), one can arrive at a relation linking  $\Gamma_1$  and  $\Gamma_2$ :  $360^\circ = (n_1 + n_2)\Gamma_1 - n_2\Gamma_2$ .

The dependence of angle parameters  $\Gamma_1, \Gamma_2$  on reduced helix radius  $R/d$  is displayed in Fig. 5, for  $\Theta < 30^\circ$  in single helix ( $n_2 = 1, n_1 \geq 4$ ), double helix ( $n_2 = 2, n_1 \geq n_2$ ) and quadruple helix ( $n_2 = 4, n_1 \geq n_2$ ).

As helix radius  $R/d$  increases, value of  $\Gamma_1$  monotonically decreases, since additional particles are added to a turn. The angular parameter  $\Gamma_2$  monotonically decreases only for  $n_2 = 1$ . The scenario becomes qualitatively different at  $n_2 \geq 2$  where non-monotonic behavior is found, see Fig. 5. This feature can be rationalized as follows. The smallest compatible radii  $R$  with  $n_2 \geq 2$  and  $\Theta < 30^\circ$ , are obtained when  $n_1 = n_2$  (cf. Fig. 4) corresponding to Z tubes where  $\Gamma_2 = 0$ . Besides that,  $\Gamma_2$  tends to zero for vanishing cylinder curvature ( $R/d \rightarrow \infty$ ). These are the reasons why the profile of  $\Gamma_2(R/d)$  is non-monotonic when  $n_2 \geq 2$ .

Surface packing fraction of densely packed multiple helices is simply obtained by multiplying the surface packing fraction of a single helix with the number of threads  $n_2$  ( $\eta_{multi} = n_2\eta$ , see Eq.1):

$$\eta_{multi} = n_2 \frac{d^2}{8\Delta z_1 R}, \quad (8)$$

where elevation distance  $\Delta z_1$  (shown in Fig. 3b) is given by:

$$\Delta z_1 = \sqrt{d^2 - 4R^2 \sin^2 \left( \frac{\Gamma_1}{2} \right)}. \quad (9)$$

The calculated surface packing fraction of a single ( $n_2 = 1$ ), double ( $n_2 = 2$ ), and quadruple ( $n_2 = 4$ ) helices is shown in Fig. 6. At given confinement curvature (fixed  $R/d$ ) adding threads results in higher surface packing fraction, see Fig. 6.

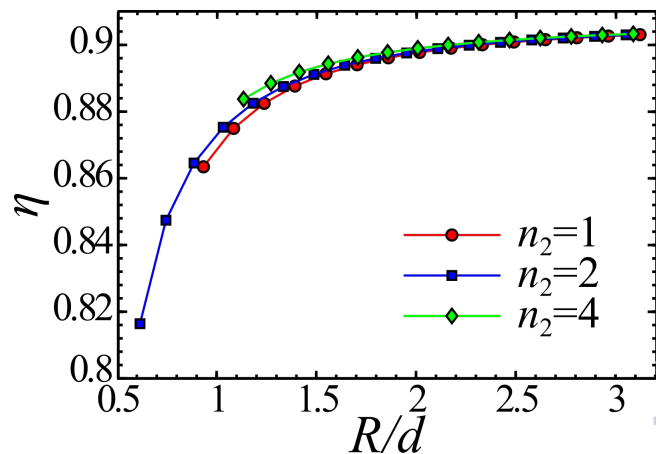


**Fig. 6** Surface packing fraction  $\eta$ , see Eq. 8 as a function of reduced helix radius  $R/d$  for single ( $n_2 = 1$ ), double ( $n_2 = 2$ ), and quadruple ( $n_2 = 4$ ) helix.

### 3 Dipole moments

#### 3.1 Dipolar interaction model

We now want to address the situation where the constitutive particles are dipolar. Each particle carries identical dipole moment in magnitude,  $m = |\vec{m}_i|$ , where  $\vec{m}_i = (m_i^x, m_i^y, m_i^z)$  defines the dipole moment of particle  $i$ , see also Fig. 1. The potential energy of interaction  $U(\vec{r}_{ij})$  between two point-like dipoles whose centers are located at  $\vec{r}_i$  and  $\vec{r}_j$  can be written as:

$$U(\vec{r}_{ij}) = C \frac{1}{r_{ij}^3} \left[ \vec{m}_i \cdot \vec{m}_j - 3 \frac{(\vec{m}_i \cdot \vec{r}_{ij})(\vec{m}_j \cdot \vec{r}_{ij})}{r_{ij}^2} \right] \quad (10)$$

for  $r_{ij} \geq d$  or  $\infty$  otherwise, where  $C$  represents a constant that depends on the intervening medium, and  $r_{ij} = |\vec{r}_{ij}| = |\vec{r}_j - \vec{r}_i|$ . It is convenient to introduce the energy scale defined by  $U_{\uparrow\uparrow} \equiv Cm^2/\omega^2$  that physically represents the repulsive potential value for two parallel dipoles at contact standing side by side as clearly suggested by the notation. Thereby, the total potential energy of interaction in a given structure  $U_{tot}$  is given by

$$U_{tot} = \sum_{\substack{i,j \\ i>j}} U(\vec{r}_{ij}). \quad (11)$$

One can then define reduced potential energy of interaction  $u$  (per particle) of  $N$  magnetic spheres. It reads  $u = U_{tot} / (U_{\uparrow\uparrow}N)$ , which will be referred to as the *cohesive energy*.

Since we are dealing with infinitely long structures (in one direction), we shall consider only periodic structures in that direction that greatly facilitates the calculation of the cohesive energy. The method of choice is provided by the Lekner sum for systems with periodicity in one direction<sup>39</sup>. The central feature in the

Lekner method is the choice of the periodic cell. For  $n_c = 2, 4$  we can always find helix parameters with a finite number of particles in the unit cell. The periodicity is achieved by imposing a condition on angular shift  $\Gamma$  that a helix has to make complete number of turns within the unit cell.

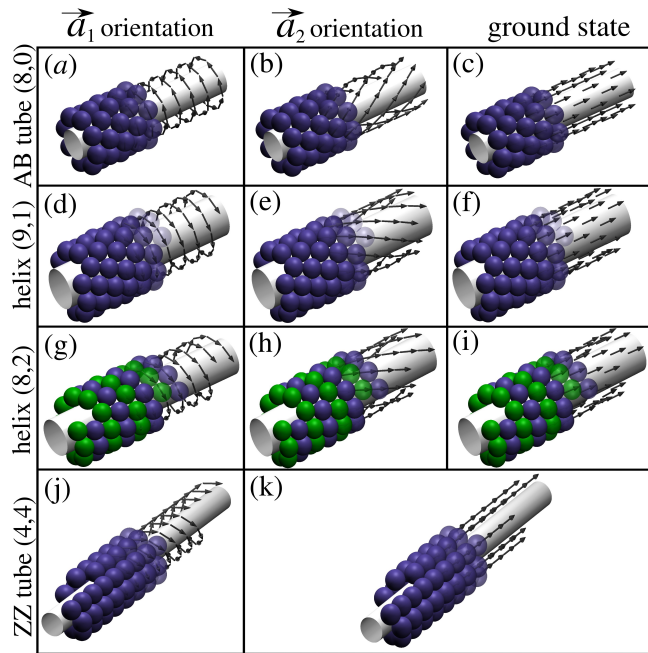


**Fig. 7** The representative structures including dipole moment distributions are displayed. For AB tube with patch parameters  $(n_1, n_2) = (8, 0)$  dipole distributions which correspond to spanning unit cell vectors (a)  $\vec{a}_1$  (oblique to cylinder's axis), (b)  $\vec{a}_2$  (closer to cylinder's axes), as well as, (c) ground state dipole distribution. For single helix  $(n_1, n_2) = (9, 1)$  dipole distributions which correspond to (d)  $\vec{a}_1$  and (e)  $\vec{a}_2$  (closer to helix axes) spanning vectors, as well as, (f) ground state dipole distribution. For double helix  $(n_1, n_2) = (8, 2)$  dipole distributions which correspond to (g)  $\vec{a}_1$ , (h)  $\vec{a}_2$  (closer to helix axes) spanning vectors, and (i) ground state dipole distribution. In case of ZZ tube (j)  $\vec{a}_1$  and (k)  $\vec{a}_2$  dipole distributions are shown. Ground state of ZZ tube follows  $\vec{a}_2$  dipole distribution (parallel to cylinder's axis).

### 3.2 Dipole moment orientation prescribed by helix threads

Because of the symmetry reason, it is intuitive to envision dipole moments following helix threads. In order to have dipole moments tangential to the helical backbone, we introduce two components of dipole moments. The parallel component with respect to helix axis is given by  $m^z = m\Delta z/d$  and the orthogonal one is given by  $|\vec{m}^{xy}| = m\sqrt{1 - (\Delta z/d)^2}$ . Hence, dipole moment of particle  $i$  in the *single thread* helix reads:  $m_i^x = -m^{xy}\sin(i\Gamma)$ ,  $m_i^y = m^{xy}\cos(i\Gamma)$ , and  $m_i^z = m_z$ .

In the *multi-thread* case, the Cartesian dipole moment compo-

nents are given by:

$$\begin{aligned} m_{i,j}^x &= -m^{xy}\sin(i\Gamma_1 + j\Gamma_2) \\ m_{i,j}^y &= m^{xy}\cos(i\Gamma_1 + j\Gamma_2) \\ m_{i,j}^z &= m\Delta z/d, \end{aligned} \quad (12)$$

where  $i \in Z$  is internal particle label within a thread and  $j = \{1, n_2\}$  stands for the thread's label. In dense helices ( $n_c = 4, 6$ ) dipole moments can follow two directions  $\vec{a}_1$  and  $\vec{a}_2$ . In Fig. 7, representative dipole moment distributions are shown.

### 3.3 Energy minimization

In general, the dipole moments do not have to follow thread structure. To find the dipole moment distribution that yields minimal energy, we first perform minimization of the cohesive energy using a constrained minimization algorithm<sup>24,40</sup>. A randomly oriented dipole moment is assigned to every particle of the helical structure in the following way: Dipole moment is defined in the spherical coordinate system. Two important features stemming from these energy minimization calculations are:

- (i) Dipole moments are tangential to the cylinder's surface.
- (ii) The component of dipole moment in the z-axis direction  $m_z$  for a given structure is identical for all particles. ||

Therefore we need just one angular parameter to characterize the dipole moment orientation. We choose the dipole moment angular parameter,  $\alpha \in [-180^\circ, 180^\circ]$  relative to z-axis, see Fig. 1. Doing so we arrive at:

$$\begin{aligned} m_{i,j}^x &= -m\sin(\alpha)\sin(i\Gamma_1 + j\Gamma_2) \\ m_{i,j}^y &= m\sin(\alpha)\cos(i\Gamma_1 + j\Gamma_2) \\ m_{i,j}^z &= m\cos(\alpha), \end{aligned} \quad (13)$$

where the indices  $i$  and  $j$  have the same meaning as in Eq. 12. Consequently, the angular parameter  $\alpha$  is most of the time unique variable, at prescribed helical structures, entering into the energy minimization routine.

## 4 Cohesion energy and microstructure

### 4.1 Compression of a single helix

A simple way to deform a helix is to compress (or extend) it along its axis, i.e.,  $z$ -direction, while ensuring the dipole moments fol-

|| We have found that under some circumstances the dipole moment orientations alternate, i.e., antiferromagnetic like coupling, between the neighboring threads. This actually occurs with any AA tube. Similar behavior is reported for some moderately dense  $n_c = 4$ -helical structures.

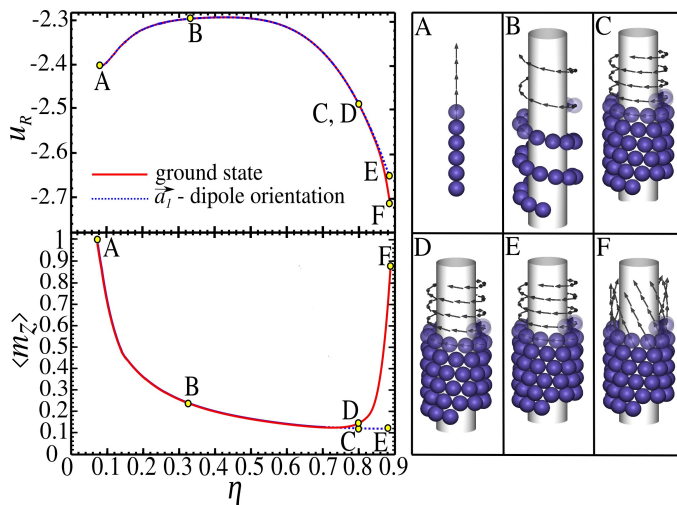


**Fig. 8** Compression of single helix on a cylindrical confinement with fixed radius ( $R/d \approx 1.7$ ). Dependence of cohesive energy (upper left panel) and overall polarization order parameter, i.e., axial component of the dipole moment (in lower left panel), on packing fraction is shown for two characteristic dipole moment orientations: one that follows the helix, i.e., spanning vector  $\vec{a}_1$ , and ground state dipole moment orientation obtained by energy minimization. Comparative microstructures at different  $\eta$  values (A-F) are depicted on the right panel. Configurations (A,B,C,E) correspond to a dipole moment distribution following the helix whereas configurations D and F correspond to ground state distributions.

low the thread (for details of implementation see Sec. 3.2). Compression of a helix results in a continuous increase of its surface packing fraction  $\eta$ . Figure 8 shows the evolution of cohesive energy  $u_R$  with surface packing fraction  $\eta$  for a single helix with reduced radius ( $R/d \approx 1.7$ , chosen in the vicinity of  $n_c = 6$  point). Recalling geometrical considerations in Sec. 2.1 increase of azimuthal angular shift  $\Gamma$  at prescribed curvature results in a continuous decrease of  $\Delta z$  and compression of the helix. The compression process begins with a fully extended helix (i.e.,  $\eta \rightarrow d/8R \approx 0.073$ ) where the chain stands up with  $\Delta z/d = 1$ , and cohesive energy of infinite chain  $u \approx -2.404^{24}$ . The compression ends when two successive turns of the helix touch, i.e., coordination number of particles in the helix changes from  $n_c = 2$  to  $n_c = 4$ .

We also address the minimal energy of the helix with respect to the dipole moment distribution (i.e., not necessarily prescribed by tangentially following the helix). From Figure 8, we observe that  $u_R = u_R(\eta)$  is non-monotonic. We can identify two regimes:

- At small packing fractions up to  $\eta \lesssim 0.4$  (with no touching turns), the compression of the helix requires energy input and therefore cohesive energy increases. The reason for this is that two distant consecutive turns of the helix experience weaker attraction upon increasing  $\eta$ .
- In the regime of high  $\eta \gtrsim 0.4$  where successive turns are allowed to be close or even touching, the cohesive energy starts to decrease as  $\eta$  increases, i.e., the helix would compress on its own without input of energy. This a consequence of an enhanced attraction due to the discreteness of the constitutive dipolar beads, see Ref.<sup>41</sup>.

The overall polarization order parameter  $\langle m_z \rangle$  is also analysed in Fig. 8. During most of the course of the helix compression,

see Fig. 8, a dipole moment orientation following the helix corresponds to the ground state structure up to  $\eta \approx 0.8$ , cf. points C and D in Fig. 8 (for details of ground state calculations see Sec. 3.3). Only for very high packing fractions, i.e.,  $\eta > 0.8$ , the ground state dipole orientation starts to rapidly deviate from the helix direction accompanied by a significant reduction in cohesive energy (see points E and F in Fig. 8). The highest difference in  $\langle m_z \rangle$  occurs for  $\eta \approx 0.887$ , where  $n_c = 4$  helix with touching turns is formed, and energy difference  $u_R^E - u_R^F \approx 0.06$ .

#### 4.2 From square to triangular arrangement for a single helix

Having successfully parameterized helices and introduced dipole moments, it is natural to ask how cohesive energy depends on structural changes and especially on curvature. With increasing curvature the structure will change from triangular to square arrangement and vice versa through a continuous series of rhombi configurations. We study first in detail systems with dipole moments following the spanning vector that are most oblique to helix axes, see Fig. 7d. For the sake of comparison with tubes (AA/A<sub>1</sub> tubes), we also chose dipole moments that are building vortices along the rings for them, cf. Fig 7a. Motivation for that choice stems from a previous study<sup>24</sup>, where we have shown that finite AB tubular systems are energetically favorable, see Fig. 7a (dipole moment orientation is perpendicular to tube's axis).

The surface packing fraction  $\eta$  (Eq. 1), angular coordination order parameter  $\xi$  (see Eq. 3), and cohesive energy per particle  $u_R$  (Eq. 11), are plotted versus reduced helix radius  $R/d$  in Fig. 9. Actually, the energy and structural properties are changing in an oscillatory quasi-periodic manner and they are enveloped from both sides with the properties of AA and AB tubes, see Fig. 9. In Fig. 10 behavior of these observables is depicted within one period ( $R/d \in [2.09, 2.26]$ , arbitrary chosen). In one period, the number of particles ( $n$ ) in a constitutive ring of (AA/AB) tubes

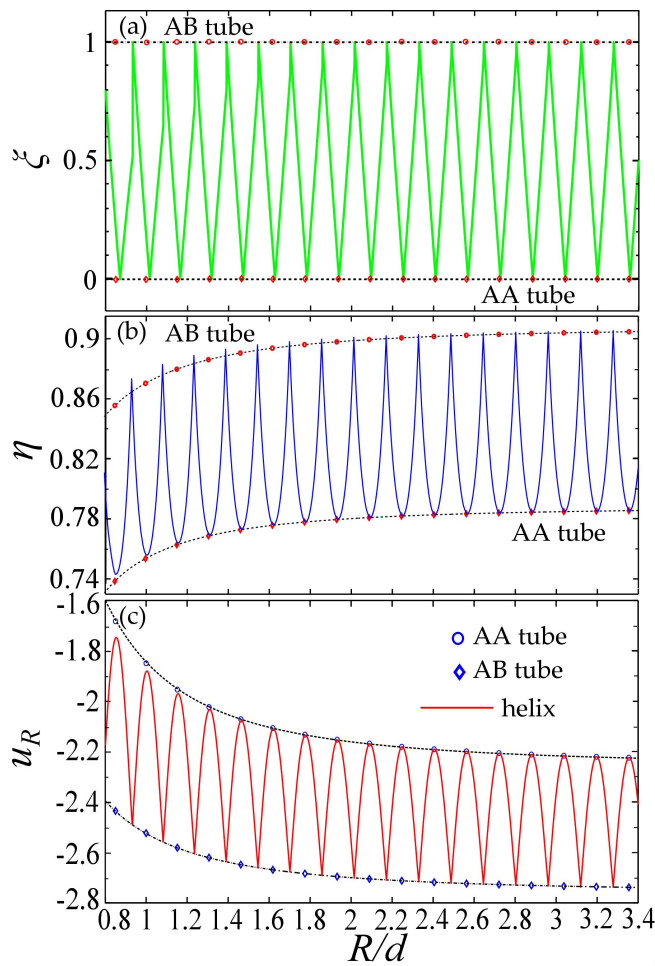


**Fig. 9** Dependence of (a) angular coordination order parameter  $\xi$ , (b) packing density  $\eta$  and (c) cohesive energy  $u_R$  on helix radius  $R/d$ , for  $\vec{\alpha}_1$  dipole orientation. AA and AB tube points are clearly indicated, they bracket the parameter values of helices, like a kind of envelopes (solid and dashed lines connecting the tube points are power law fits).

is increased for one, i.e., from  $n$ -ring to  $n+1$ -ring. Within this period, order parameter is changing from  $\xi = 0$ , i.e., square arrangement, to  $\xi = 1$ , i.e., triangular arrangement, via continuous rhombic transformation, see Fig. 10a. The radii of densely packed helices are roughly in the middle between two corresponding (AB/AA) tube radii, see Fig. 10a. This is a result of the radial constraint and excluded volume. Though in a single thread helical structure we cannot close rings in the perpendicular plane to the cylinder axis, one can nevertheless realize a full  $360^\circ$  helix turn with roughly  $n+1/2$  particles. We observe discontinuity and strong asymmetry of angular coordination order parameter  $\xi$  at mid period ( $R_{(13,1)}/d \approx 2.17$ ), see Fig. 10a. This is due to a change of the number of lateral threads  $n_2$ , see for illustration Fig. 7e, at mid period going from  $n_2 = 9$  to  $n_2 = 10$ , see Fig. 10a.

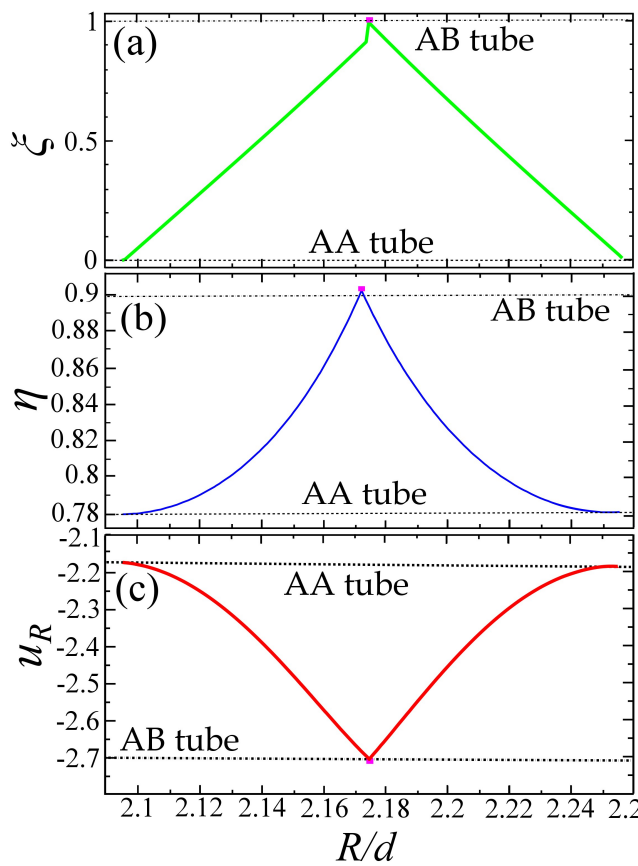


**Fig. 10** Dependence of (a) angular coordination order parameter  $\xi$ , (b) packing density  $\eta$  and (c) cohesive energy  $u_R$  on helix radius  $R/d$ , for a segment in vicinity of  $R_{(13,1)}/d = 2.17$  of Fig. 9. Tubes AA and AB are represented with discrete points since they can be formed only with a fixed number of particles in a ring, the fitted (power law) curves serve only as a guide to the eye. The point which represents the dense helix with  $(n_1, n_2) = (13, 1)$  and  $R_{(13,1)}/d = 2.17$ , is marked with a rectangle.

With decreasing curvature, surface packing fraction is globally increasing, see Fig. 9b. We observe oscillatory behavior as system continuously evolves from square to triangular arrangement and vice versa. The AA and AB tubes still roughly bound the values taken by surface packing fraction. At helix radius  $R/d > 3.4$ , see Fig. 9b, we are already within 3% of the asymptotic expected values in the *planar case*. In contrast to angular coordination parameter  $\xi$ , surface packing density  $\eta$  is everywhere continuous, compare Figs. 10a and b. Moreover, at mid-period the  $\eta$  value is slightly (and systematically, see Fig. 9b,) above the interpolated stemming from AB tubes (see Fig. 10b). In Fig. 9b and c, it can be clearly seen that the profiles of energy oscillations  $u_R$  and surface packing fraction  $\eta$  are anti-correlated. The mid-period values  $u_R$  coincide with interpolated stemming from AB tube radii

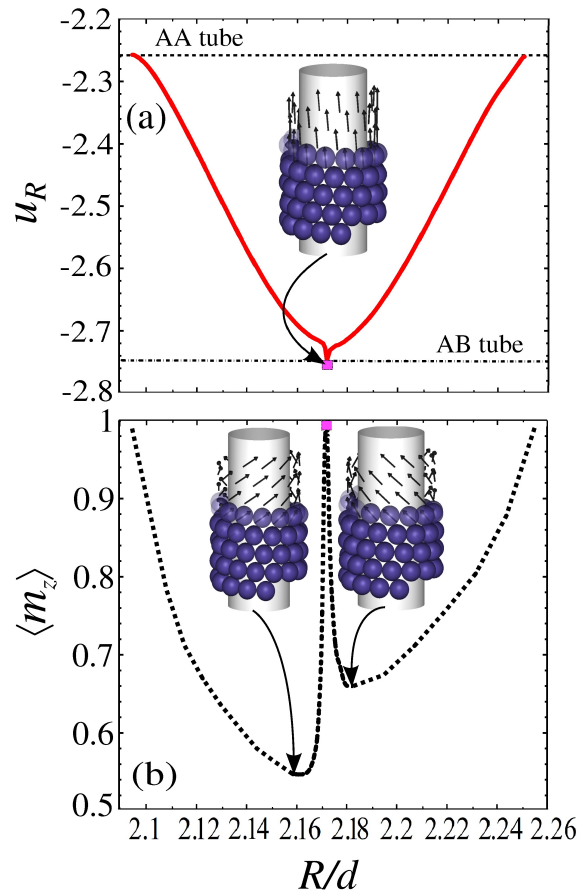


**Fig. 11** Dependence of (a) cohesive energy  $u_R$ , and (b) overall polarization order parameter  $\langle m_z \rangle$  on helix radius  $R/d$  (in the ground state), for a chosen segment of Fig. 9. Tubes AA and AB are represented with discrete points since they can be formed only with a fixed number of particles in a ring, the fitted (power law) curves serve only as a guide to the eye. The point which represents the dense helix with  $(n_1, n_2) = (13, 1)$  and  $R_{(13,1)}/d = 2.17$ , is marked with a rectangle.

(confirmed by Figs. 9c and 10c).

#### 4.3 Looking for the ground state

At this point, we would like to discuss mechanisms which govern the minimal energy dipole moment orientation near mid-period transition point (more detail about implementation is provided in Sec. 3.3). There are three privileged directions in a helix: two which follow helix spanning vectors (determined by  $\vec{a}_1, \vec{a}_2$ ) and the third one which is the direction of the helix axis. These privileged directions come into play in two competing mechanisms:

- The first mechanism is typically dictated by first neighbor interactions which favors dipole moments following the thread directions.

- The distant-neighbor interactions favor distribution of dipole moments parallel to the helix axis.

We can justify these two mechanisms as follows. It is well known for small finite system that rings are formed with dipole moments building vortices, cf. Ref.<sup>24</sup>. When a helix turn is projected along z-axis, the resulting figure is highly reminiscent of the vortex discussed above. The head to tail configuration is favored at long distances, explaining the second advocated mechanism.

The abrupt change of polarization (or magnetization) in direction of axis  $\langle m_z \rangle$ , seen in Fig 11b, is correlated with the discontinuous change in angular coordination order parameter  $\xi$  in the vicinity of transition, see Fig. 10a. At the mid-period point  $R_{(13,1)}/d = 2.17$  magnetization in direction of axis  $\langle m_z \rangle$  is close to one, but not exactly one, see Fig. 11.

For the sake of comparison with tubes (AA/AB tubes), we choose dipole moments that are parallel with the helix axis, see Fig 7c. Fact that the system is able to relax its dipole moment orientation to the ground state results in a more dependence of energy on confinement curvature around mid point. The degree of asymmetry of the  $u_R$  is stronger around transition point, see Fig. 11b, than in the excited state in Fig. 10c. The ground state calculations, confirm the high stability of AB tubes (see Fig. 10c)

#### 4.4 Cohesion energy for multiple helices at high surface packing fraction

In this part, we consider the high surface packing fraction regime with  $n_c = 6$ . Some representative structures including dipole moment streamlines are displayed in Fig. 7. The streamlines following spanning unit cell vectors  $\vec{a}_1$  (oblique to helix axis) and  $\vec{a}_2$  (more aligned to helix axis) are also shown \*\*. Dipole moment distributions in the ground states are also indicated for comparison in Fig. 7. In analogy to the study of single helix case (see Sec. 4.2), we start analysis with a dipole moment distribution prescribed by tangentiality with thread backbone. In Fig. 12 cohesive energy for  $\vec{a}_1$ -generated dipole moment distribution is shown for different helical structures.

The cohesive energy in a planar triangular lattice,  $u_\infty \simeq -2.75$ , represents the energy value which will be reached asymptotically ( $R/d \rightarrow \infty$ ) for all considered structures. As already found for AP tubes in Ref.<sup>24</sup>, cohesive energy exhibits scaling law of the form  $u_R - u_\infty \sim R^{-2}$ , see Fig. 12. The cohesive energies of all three helices and AB tube are weakly dependent on number of threads for  $\vec{a}_1$ -generated dipole moment distribution. This is in accordance

\*\* It is possible to polarize the helix by an homogeneous external field parallel to its axis. For symmetry reasons, a reversal of the magnetic field should result in reversal of the dipole orientation. In case of magnetic dipoles, it should also be possible to polarize system to follow  $\vec{a}_1$  and  $\vec{a}_2$  spanning vectors by combination of curling magnetic field of electric current flowing through the confining cylinder and homogeneous external magnetic field parallel to its axis.

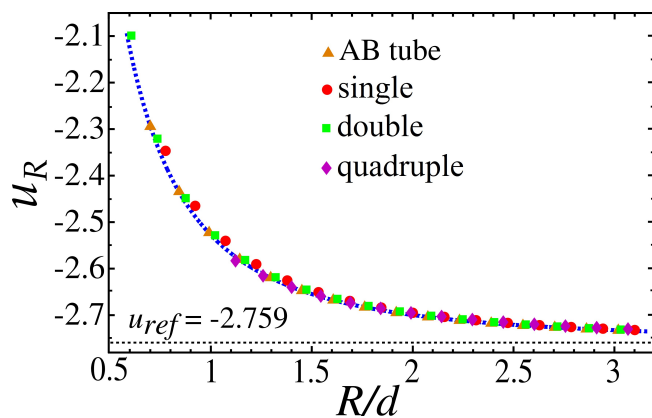


**Fig. 12** Dependence of cohesive energy  $u_R$  on helix radius  $R/d$ , for single, double, and quadruple helices at high surface packing fraction, and AB tubes, with  $\vec{a}_1$  dipole orientation.

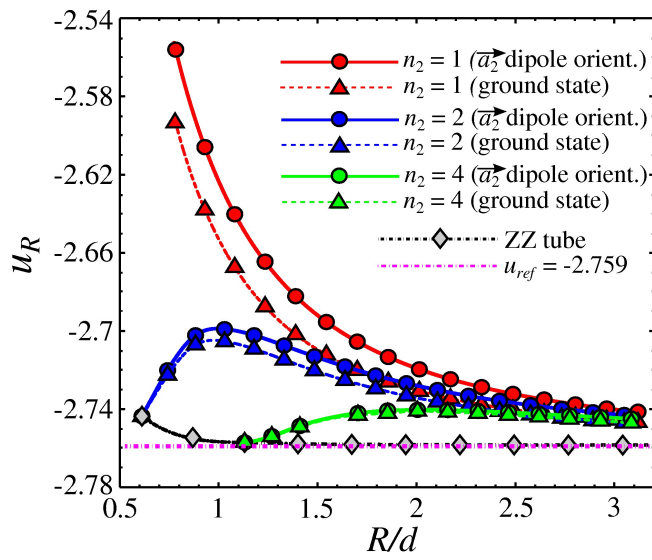


**Fig. 13** Dependence of cohesive energy  $u_R$  on helix radius  $R/d$ , for families of single, double, and quadruple helices at high surface packing fraction, i.e.,  $n_2 = \{1, 2, 4\}$ , respectively, and AB tubes, with  $\vec{a}_2$  and optimized dipole moment orientation.

to surface packing fraction behavior reported in Fig. 6. A comparison with azimuthal angular shift parameter  $\Gamma_1$ , see Fig. 5, and corresponding cohesive energy (for  $\vec{a}_1$ -generated dipole moment distribution) clearly reveals a correlation between these two quantities.

In Fig. 13, cohesive energy for  $\vec{a}_2$ -generated dipole moment distribution is compared with ground state energy for different number of threads. There exists an analogous correlation (as discussed for  $\vec{a}_1$ -dipole distribution) between azimuthal shift  $\Gamma_2$  and resulting cohesive energy, compare Figs. 5 and 13.

The smallest compatible radius  $R$  for multi thread helices ( $n_2 = 2, 4$ ) is obtained for ZZ tubes ( $n_1 = n_2$ ). In Fig. 13, the corresponding radii read  $R_{(2,2)}/d = 0.61$  and  $R_{(4,4)}/d = 1.13$ . In this case the  $\vec{a}_2$  and ground state dipole moment orientations are the same, see Fig. 7k. Strikingly, ZZ tube ground states converge very fast to the expected planar value  $u_\infty$  at the smallest accessible radii, i.e., largest curvature, within less than 1% of the planar case, see Fig. 13 for  $R_{(2,2)}/d = 0.61$ . A structural similarity of ZZ tubes, with typical experimental images of microtubules is striking, see Fig. 7k. Structurally, ZZ tubes can be created by closing of rectangular strip on a cylinder and decomposed into chains which are analogous to biological filaments which the microtubules are made of.

## 5 Conclusions

We have presented a study about cohesive energy of helical structures composed of hard spheres with permanent dipole moments. Helices were created by replication of a particle or patch (of particles) on a confining cylindrical surface. Even for the most simple situation, namely the single thread helix, a non-trivial behavior is found when monitoring the cohesive energy as a function of surface packing (i.e., axial compression). In particular, we observe a *non-monotonic* dependence of the cohesive energy on packing fraction (or equivalently amount of compression) as a result of a delicate interplay of dipole-dipole interactions and excluded volume effects. Lowest cohesive energy is achieved at the highest packing fraction with touching turns. In parallel, the magnetization (or polarization) order parameter, i.e., the mean dipole moment per particle in the  $\langle m_z \rangle$ , also exhibits a striking non-monotonic behavior as a function of compression amount. In the regime of very high surface packing fraction with local triangular arrangement compatible with certain cylinder radius ( $R$ ) vs particle diameter ( $d$ ) ratio ( $R/d$ ), a pronounced cohesive energy is found. Concomitantly, the magnetization order parameter indicates a sharp change in the dipole moment orientation, tending to be parallel with the helix axis.

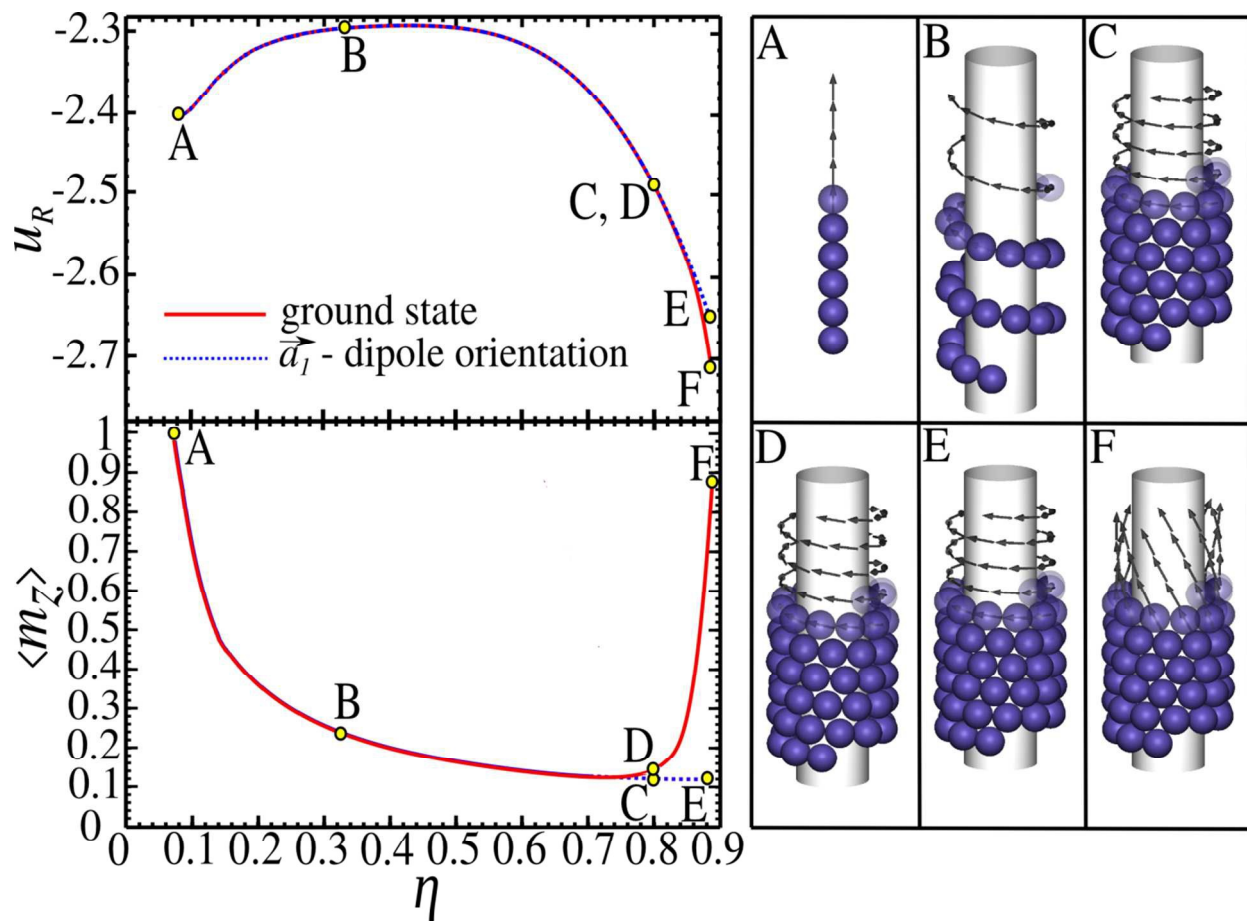
Finally, we compare cohesive energies of dense multiple (i.e., double or quadruple) helices, as well as, AB and ZZ-tubes made up of stacking rings that can also be seen as special multiple helices. A remarkable finding is the enhanced cohesive energy for the ZZ-tube structure. The latter already emerges at strong substrate curvature with cohesive energies very close to that obtained at vanishing curvatures. In these ZZ-tube structures, an alignment of the helix threads with its axis is a microstructural signature for this low cohesive energy. As a final note, we would like to emphasize that our model mimics nicely the geometry and microstructure of microtubules. It could also provide a possible clue about the self-assembly mechanisms and cohesion within microtubular structures.

## 6 Acknowledgements

The authors acknowledge financial support from the bilateral Franco-Serbian PHC Pavle Savic 2014/15 program (No. 32135NJ). I.S. and M.D. acknowledge support received from the Serbian Ministry of Education and Science (Grants No. ON171017 and No. III45018). Numerical calculations were run on the PARADOX supercomputing facility at the Scientific Computing Laboratory of the Institute of Physics Belgrade.

## References

- 1 W. Wen, N. Wang, D. W. Zheng, C. Chen and K. N. Tu, *J. Mater. Res.*, 1999, **14**, 1186–1189.
- 2 D. J. Sellmyer, *Nature*, 2002, **420**, 374–375.
- 3 G. M. Whitesides and B. Grzybowski, *Science*, 2002, **295**, 2418–2421.
- 4 K. F. Jarrell and M. J. McBride, *Nat. Rev. Microbiol.*, 2008, **6**, 466–476.
- 5 I. M. Cheeseman and A. Desai, *Nat. Rev. Mol. Cell. Biol.*, 2008, **9**, 33–46.
- 6 J. Howard and A. A. Hyman, *Nat. Rev. Microbiol.*, 2009, **10**, 569–574.
- 7 D. V. Kosynkin, A. L. Higginbotham, A. Sinitskii, J. R. Lomeda, A. Dimiev, B. K. Price and J. M. Tour, *Nature*, 2009, **458**, 872–876.
- 8 X. Zhang, X. Zhang, D. Bernaerts, G. Van Tendeloo, S. Amelinckx, J. Van Landuyt, V. Ivanov, J. Nagy, P. Lambin and A. Lucas, *EPL (Europhysics Letters)*, 1994, **27**, 141.
- 9 S. M. Douglas, J. J. Chou and W. M. Shih, *Proc. Natl. Acad. Sci. U. S. A.*, 2007, **104**, 6644–6648.
- 10 G. D. Lilly, A. Agarwal, S. Srivastava and N. A. Kotov, *Small*, 2011, **7**, 2004–2009.
- 11 T. Shimizu, M. Masuda and H. Minamikawa, *Chem. Rev.*, 2005, **105**, 1401–1444.
- 12 Y. Yamamoto, T. Fukushima, Y. Suna, N. Ishii, A. Saeki, S. Seki, S. Tagawa, M. Taniguchi, T. Kawai and T. Aida, *Science*, 2006, **314**, 1761–1764.
- 13 W. Zhuang, E. Kasemi, Y. Ding, M. Kröger, A. D. Schlüter and J. P. Rabe, *Adv. Mater.*, 2008, **20**, 3204–3210.
- 14 G. Singh, H. Chan, A. Baskin, E. Gelman, N. Repnin, P. Kral and R. Klajn, *Science*, 2014, **345**, 1149–1153.
- 15 D. Zerrouki, J. Baudry, D. Pine, P. Chaikin and J. Bibette, *Nature*, 2008, **455**, 380–382.
- 16 G. Pickett, M. Gross and H. Okuyama, *Phys. Rev. Lett.*, 2000, **85**, 3652–3655.
- 17 E. C. Oguz, R. Messina and H. Loewen, *EPL (Europhysics Letters)*, 2011, **94**, 28005.
- 18 M. A. Lohr, A. M. Alsayed, B. G. Chen, Z. Zhang, R. D. Kamien and A. G. Yodh, *Phys. Rev. E*, 2010, **81**, 040401.
- 19 A. Mershin, A. A. Kolomenski, H. A. Schuessler and D. V. Nanopoulos, *BioSystems*, 2004, **77**, 73–85.
- 20 E. D. Spoerke, G. D. Bachand, J. Liu, D. Sasaki and B. C. Bunker, *Langmuir*, 2008, **24**, 7039–7043.
- 21 M. Cifra, J. Pokorný, D. Havelka and O. Kučera, *BioSystems*, 2010, **100**, 122–131.
- 22 I. Jacobs and C. Bean, *Phys. Rev.*, 1955, **100**, 1060.
- 23 P.-G. De Gennes and P. A. Pincus, *Phys. Kondens. Mater.*, 1970, **11**, 189–198.
- 24 R. Messina, L. A. Khalil and I. Stanković, *Phys. Rev. E*, 2014, **89**, 011202.
- 25 D. Vella, E. du Pontavice, C. L. Hall and A. Goriely, *Proc. R. Soc. London Ser. A*, 2013, **470**, 20130609.
- 26 Y. Ding, H. C. Öttinger, A. D. Schlüter and M. Kröger, *J. Chem. Phys.*, 2007, **127**, 094904.
- 27 M. Kröger, O. Peleg, Y. Ding and Y. Rabin, *Soft Matter*, 2008, **4**, 18–28.
- 28 T. X. Hoang, A. Giacometti, R. Podgornik, N. T. Nguyen, J. D. Banavar and A. Maritan, *J. Chem. Phys.*, 2014, **140**, 064902.
- 29 R. Cortini, B. R. Caré, J.-M. Victor and M. Barbi, *J. Chem. Phys.*, 2015, **142**, 105102.
- 30 H. Mohrbach, A. Johner and I. M. Kulić, *Phys. Rev. Lett.*, 2010, **105**, 268102.
- 31 O. Kahraman, H. Mohrbach, M. M. Müller and I. M. Kulić, *Soft Matter*, 2014, **10**, 2836–2847.
- 32 D. Tomanek, S. G. Kim, P. Jund, P. Borrmann, H. Stamerjohanns and E. R. Hilf, *Z. Phys. D: Atoms, Molecules and Clusters*, 1997, **40**, 539–541.
- 33 T. A. Prokopieva, V. A. Danilov, S. S. Kantorovich and C. Holm, *Phys. Rev. E*, 2009, **80**, 031404.
- 34 G. Pál, F. Kun, I. Varga, D. Sohler and G. Sun, *Phys. Rev. E*, 2011, **83**, 061504.
- 35 V. Malik, A. V. Petukhov, L. He, Y. Yin and M. Schmidt, *Langmuir*, 2012, **28**, 14777–14783.
- 36 N. Vandewalle and S. Dorbolo, *New J. Phys.*, 2014, **15**, 013050.
- 37 D. A. Wood, C. D. Santangelo and A. D. Dinsmore, *Soft Matter*, 2013, **9**, 10016–10024.
- 38 W. T. B. Kelvin, *The molecular tactics of a crystal*, Clarendon Press, 1894.
- 39 A. Grzybowski and A. Bródka, *Mol. Phys.*, 2003, **101**, 1079–1088.
- 40 L. Assoud and R. Messina, *Phys. Rev. E*, 2011, **83**, 036113.
- 41 R. Messina and I. Stanković, submitted to *Phys. Rev. E*.



A striking non-monotonic behavior is observed for the cohesive energy and ground state polarization order parameter as a function of the surface packing fraction. Comparative microstructures (A-F) are depicted on the right panel.